

Assessment of Surface-local Strains from Remnant Microindents on a Zr-based Metallic Glass

Yun-Hee Lee^{1,*}, Yongil Kim¹, Young-Cheon Kim², Ju-Young Kim², and Jae-il Jang³

¹Korea Research Institute of Standards and Science, Division of Industrial Metrology, Daejeon 305-340, Korea

²UNIST, School of Mechanical and Advanced Materials Engineering, Ulsan 689-798, Korea

³Hanyang University, Department of Materials Science and Engineering, Seoul 133-791, Korea

(received date: 14 August 2012 / accepted date: 28 September 2013)

In this study, a morphological modeling was done for remnant microindents on a Zr-based metallic glass for avoiding an overestimation in the indented surface area by applying the Riemann integral and for calculating quantitative values of the stretch strain which is defined by the indented surface area divided by its projected area according to Milman *et al.* A discrete pixel image for an indent was fitted into a continuous ellipsoidal cap and its indented surface area by a spherical indenter was deterministically calculated by integrating the ellipsoidal cap surface. The calculated stretch strains were lower than their upper limits and quantitatively close to the conventional indentation strains. The stretch strains were generally higher than the conventional indentation strains but decreased to their lower values at a shallow indentation of less than 50 μm . This phenomenon was attributed to severe elastic recovery in shallow indentations. From an overall viewpoint, the strain overestimation by the Riemann integral was clearly resolved, and this result confirmed the validity of the new approach for estimating the indented surface area and the stretch strain.

Key words: amorphous materials, deformation, hardness test, image analysis, indentation strain

1. INTRODUCTION

Bulk metallic glasses (BMGs) are not much used in engineering applications despite their good mechanical properties, such as a high elastic limit, high hardness and strength, and superior wear resistance, because catastrophic fracture occurs immediately after yielding due to strain localization under uniaxial tension [1]. On the other hand, little inelastic deformations accompanying multiple shear bands have been identified under uniaxial compression or bending [2–4]. Indentation tests, including the conventional hardness tests, can cause multiaxial deformation due to a significant geometrical constraint and have been frequently used for investigating the large strain behaviors of BMGs [4–11]. Especially different from the pyramidal indenters yielding a fixed strain value regardless of indentation depths, a spherical indenter forms a strain increase with increasing indentation depths, and so it is used to study the contact pressure or indentation stress as a function of indentation strain.

From spherical and sharp indentation studies in BMGs [5–11], the indentation strain has been treated from various view-

points. Patnaik *et al.* [5] proposed a modified expanding cavity model and plotted a trend of the plastic constraint beneath an indenter against the conventional indentation strain normalized with the compressive yield strain. Here the conventional indentation strain proposed by Tabor is expressed by $0.2 a/R$ [6]. The contact radius and the indenter radius are denoted by a and R , respectively. Keryvin [7] used the conventional indentation strain without modification, and Ai and Dai [8] adopted the trigonometry form of the conventional indentation strain proposed by Ahn and Kwon [9]. Tang *et al.* [10] studied the work-hardening behavior of a Zr-based metallic glass and expressed the work-hardening behavior with the Meyer relationship. Instead of the conventional indentation strain [6,9], Milman *et al.* [13] proposed a new concept for the indentation strain; since the mechanical strain means a degree of dimensional variation from the original morphology due to external loadings, the indentation strain is expressed by the degree of areal increase due to the indenter penetration and is formulated by Eq. (1).

$$\varepsilon_i = \ln\left(\frac{S_i}{S_p}\right) \quad (1)$$

The flat, original surface area S_p beneath a spherical indenter stretches to the curved, indented surface area S_i . If the con-

*Corresponding author: uni44@kriss.re.kr
©KIM and Springer

tact radius implying the pileup effect is given by c , S_p will be πc^2 and S_i can be $2\pi R(R - \sqrt{R^2 - c^2})$ corresponding to a perfect spherical contact morphology at the peak indentation load. This indentation strain indicating the degree of surface stretch due to the indentation will be denoted as the stretch strain hereafter. This stretch strain was adopted for analyzing spherical microindents formed on a Zr-based metallic glass in a previous study [14]. Although the rigid plastic characteristic of the metallic glass could be identified by deriving the pileup-corrected contact boundary, the measured stretch strains were highly overestimated compared to the conventional indentation strains. This is attributed to the side effects of the Riemann integral, which is used to calculate the indented surface area. When surface area of a slanted surface is considered, the Riemann integral makes a summation for three-exposed faces of each discrete pixel in the surface and thus exaggerate the surface area.

Thus, in this study, we tried a geometrical fitting method in order to avoid the overestimates in the indented surface area and subsequent stretch strain. A spherical indent that has undergone elastic recovery is modeled into a part of an ellipsoid, and its indented area can be easily calculated by integrating the determined ellipsoidal function. The estimated stretch strains were compared with their upper limits and the conventional indentation strains. Finally, the validity of the proposed ellipsoidal fitting was confirmed empirically.

2. MORPHOLOGICAL MODELING

A spherical indentation morphology simplified into a spherical cap undergoes complex recoveries along the indentation direction and surface-parallel directions during unloading; the recoveries cannot be even, and finally, the remnant indent may seem to an ellipsoidal cap. If a specimen does not have directionality or an-isotropy because it has single crystallinity or texture, the ellipsoidal cap representing the remnant indents has unique characteristics: both axial radii along the X- and Z-axes consisting of the specimen surface have the same value. That means that the fitted ellipsoid can be a prolate or oblate ellipsoid depending on the degree of the elastic relaxation along the Y-axis or the indentation direction. In addition, since the ellipsoidal cap originates from the spherical morphology, the ellipsoid center after the unloading can be assumed to be identical with the center of the spherical morphology at the maximum indentation depth. The cross-sectional morphology representing the relationship between the remnant indentation depth and the radius at the unloaded state is compared with the morphology showing the relationship between the indentation depth and the contact radius at the loaded state in Fig. 1.

First of all, S_p in Eq. (1) is given by πc^2 for the pileup-corrected contact radius c . The unloaded morphology is fitted into the elliptical part and forms a prolate ellipsoid by rotat-

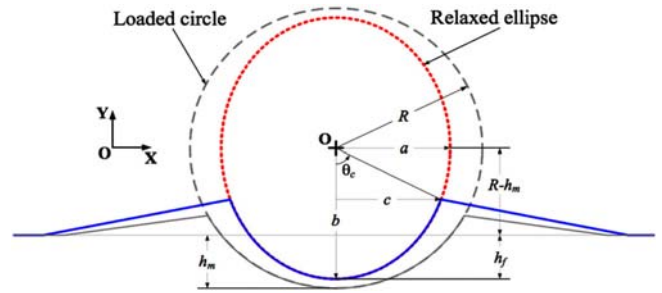


Fig. 1. Cross-sectional morphologies of a spherical indentation at loaded and unloaded states.

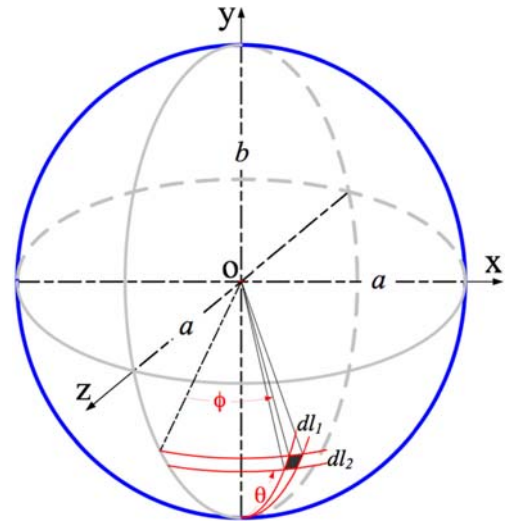


Fig. 2. A prolate ellipsoid formed by rotating the ellipse in Fig. 1 about the indentation axis.

ing the ellipse about the Y or the indentation axis (see Figs. 1 and 2).

The prolate ellipsoid formed by the ellipse revolution has the same radius along both the X- and Z-axes. From the overlapped geometries under the loaded and unloaded states, one major radius b along the Y-axis (or the indentation depth direction) can be expressed by $(R - h_{max}) + h_f$. Also the common minor radius, along both the X- and Z-axes can be formulated by Eq. (2) according to the equation of an ellipse. Here, the x_i and y_i coordinates of any point on the ellipse indicate the impression radius and the remnant indentation depth, respectively.

$$a^2 = \frac{x_i^2}{1 - \frac{(y_i - b)^2}{b^2}} \tag{2}$$

Finally, the ellipsoid fitted from a remnant impression is expressed by Eq. (3). Here, the center of the ellipsoid is given by $(0, 0, 0)$ and its revolution axis is the indentation depth direction.

$$\frac{x^2}{a^2} + \frac{y^2}{b^2} + \frac{z^2}{a^2} = 1 \quad (3)$$

The prolate ellipsoid expressed by Eq. (3) is a special case of the general ellipsoid, which was modeled by Kumar and Mathew [15]. Both line elements dl_1 and dl_2 consisting of the spherical surface element can be simplified by Eq. (4).

$$dl_1 = a \cdot \sin\theta d\phi$$

$$dl_2 = \sqrt{a^2 \cos^2\theta + b^2 \sin^2\theta} d\theta \quad (4)$$

Since the prolate ellipsoid is formed by an ellipse revolution around the Y-axis, the impression surface area S_i is given by Eq. (5).

$$S_i = \int_0^{\theta_c} \int_0^{2\pi} dl_1 \cdot dl_2$$

$$= \int_0^{\theta_c} \int_0^{2\pi} a \cdot \sin\theta \cdot \sqrt{a^2 \cos^2\theta + b^2 \sin^2\theta} d\phi d\theta$$

$$= 2\pi \int_0^{\theta_c} a \cdot \sin\theta \cdot \sqrt{a^2 \cos^2\theta + b^2 \sin^2\theta} d\theta \quad (5)$$

Here, θ is the deviation angle from the indentation axis and θ_c in Fig. 1 represents the location of the contact boundary. Thus, θ_c is determined from the empirically measured contact radius c , the center O and axial radii a and b of the fitted ellipsoid.

3. EXPERIMENTAL PROCEDURES

Bulk metallic glass Zr-10Al-5Ni-30Cu (wt%) was prepared by melting pure metal elements in an argon environment, followed by casting in a copper mold. The as-cast plate was 3 mm thick and was mechanically polished to mirror smoothness and then indented by a spherical WC-Co indenter with a curvature radius of 250 micron. A series of indentations with depths from 20 to 100 micron at a loading rate of 0.3 mm/min were carried out using an AIS 3000R system (Frontics Inc., Korea). Subsequently, three-dimensional morphologies of the microindents formed on the BMG plate were observed with a Dektak-8 profiler (Veeco Instruments Inc., USA). An engaging load of 9.8 μ N was applied on a stylus with a curvature radius of 700 nm. Through an interpolation between scanning lines, the remnant indent image was converted into an ASCII file in the form of a square matrix having 256×256 pixels and then the square matrix was used for Matlab[®] image analysis.

4. RESULTS AND DISCUSSION

4.1. Determinations for the pileup-corrected contact radius

In this study, apart from the conventional analysis for indentation load-displacement curves [16], we also conducted morphological investigations for spherical microindents. From the contour graph of a remnant indent in Fig. 3, pileup defor-

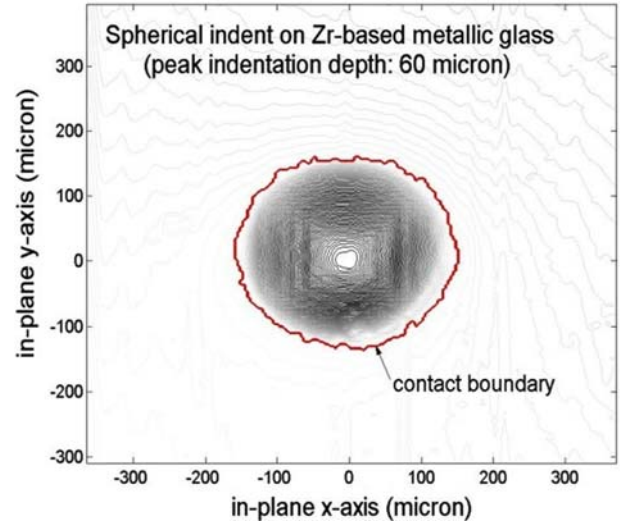


Fig. 3. Contour plot for a remnant microindent formed on the Zr-based metallic glass.

mation is clearly identified and thus a pileup correction is needed for determining the contacted region. According to previous studies [17-21], the contact boundary is determined differently for the sinkin-dominant and pileup-dominant indents; while the fastest slope change is traced inside of the sinkin-dominant indents [17,18], few peak points in the pileup region is traced for the pileup-dominant indents [19-21]. However, only a few pileup peaks were not enough to form the actual contact boundary and thus the radial differentiation method producing the contact boundary as a closed loop was proposed by Lee *et al.* [22]. Variation of surface height along the radial direction from the center or origin of the spherical indent was differentiated with distance from the origin. The points with a first order differentiation value of zero formed the contact boundary of each microindent [22]. By integrating the area enveloped by the contact boundary, the pileup-corrected contact area symbolized as S_p in Eq. (1) was calculated and subsequently converted to the contact radius c .

4.2. Overestimations in the indented surface area and the Riemann stretch strain

From the Riemann integral inside of the contacted area S_p , the indented surface area S_i was estimated in our previous study [14]. The Riemann stretch strains were calculated from S_i and area S_p values by Eq. (1) and were 4 to 7 times higher than the conventional indentation strains [6] estimated from the contact mechanical analysis for raw indentation curves [16] (see Fig. 4). From now on, the indentation strain calculated by the Riemann integral will be denoted by the Riemann stretch strain to distinguish it from the stretch strain that is evaluated through the ellipsoidal model in this study. Although the indentation stress-strain data showed a rigid plasticity of the Zr-based metallic glass, the strain values seem to be overes-

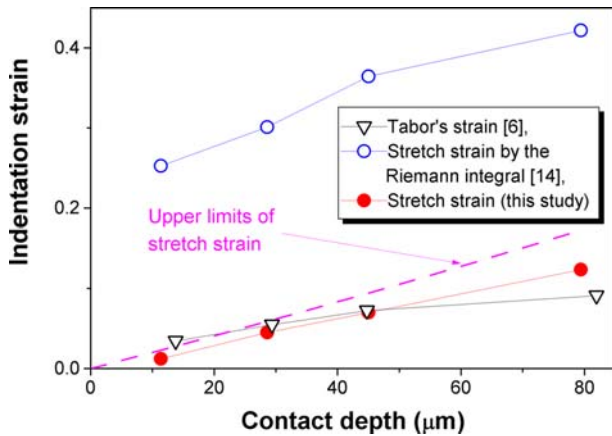


Fig. 4. Comparison of the stretch strains from the ellipsoidal fitting model with other indentation strains [6,14].

timated; the degree of the overestimation cannot be measured quantitatively because absolute, real values of the indentation strain cannot be evaluated at the current research step. Thus, the stretch strains were compared with their upper limits in this study. The upper strain limit of an indentation corresponds to the largest deformation or spherical indenting morphology beneath the spherical indenter. Both equations for the indented surface area and its projected contact area of a spherical indenting morphology were given by $2\pi R(R - \sqrt{R^2 - c^2})$ and πc^2 , respectively. For the spherical indentation with a curvature radius of 250 μm , the upper strain limits were plotted as a continuous curve shown as a dashed line in Fig. 4. From a quantitative viewpoint, the Riemann stretch strains were 2.6 to 18 times higher than the upper strain limits for spherical contact geometry. We attribute this phenomenon to the area overestimation in the Riemann integral.

4.3. Stretch strains estimated from the ellipsoid fittings for remnant indents

In order to calculate the actual stretch strains, 3D morphologies of the remnant indents were fitted into the prolate ellipsoid modeled in Section 2. In detail, a cross-sectional plane parallel to the sample surface was introduced to the 3D indent morphology at a given depth below the pileup-corrected contact depth. This morphological overlap resulted in a closed contact area at a given depth h . By deriving the effective circular area from the contact area, the contact radius r was calculated (see Fig. 5). By repeating this morphological overlap for all indentation depths, the plot between contact radius r and indentation depth h was constructed for a spherical indent as shown in Fig. 5. This figure exactly represents the part of the indent ellipse formed by projecting the 3D fitted ellipsoid on the X-Y plane. From the information on the indenter radius and the peak and final indentation depths of each indent, the semi-minor radius was determined according to the ellipsoidal model in Section 2. Moreover, the semi-major

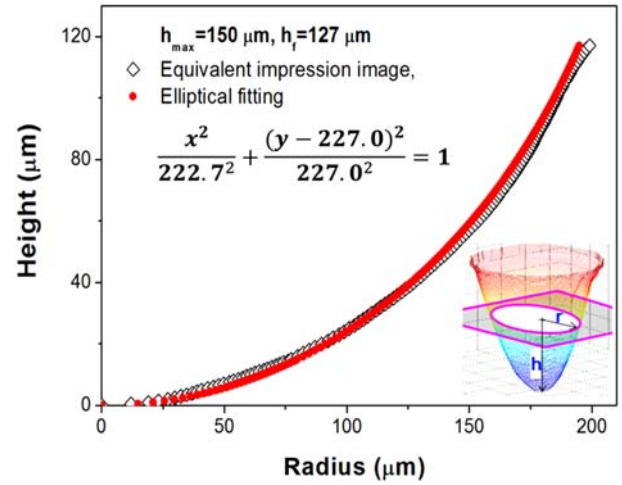


Fig. 5. Elliptical fitting through a 3D image analysis for a microindent.

radius of the indent ellipse was optimized by inputting the r, h coordinates of all points on the ellipse part in Fig. 5 into Eq. (2).

Finally, the morphological equation for the prolate ellipsoid in Eq. (3) was derived for each microindent using the determined radii. The indented surface area and its projected area were calculated from Eq. (5) and the predetermined contact area, respectively, for the fitted ellipsoidal cap and used for calculating the stretch strain in Eq. (1). The final stretch strains were calculated from the empirically fitted ellipsoids corresponding to all spherical microindents and overlapped as solid circles in Fig. 4. The stretch strains were located below their upper limits shown as the dashed line and were close to the conventional indentation strains. For small microindents shallower than 50 μm , the stretch strains were lower than the conventional indentation strains. A similar hardness trend in shallow indentations was reported in a previous study [22]. The contact area analyzed from the remnant indent image was smaller than that analyzed from the indentation load-displacement curve due to a severe elastic recovery at shallow indentations. Similarly, a large contact can be obtained at the peak indentation load compared with its relaxed contact morphology at the unloaded state at shallow indentations implying significant elastic deformation. Thus the Tabor's strains [6] calculated based on the contact properties from the unloading curve analysis [16] have higher strain values than the stretch strains from the unloaded microindents. This strain trend was reversed at deep indentations above 50 μm . As might be expected, the stretch strain was located in a middle range of the conventional indentation strains and the strain upper limits. From an overall viewpoint, the strain overestimation by the Riemann integral was clearly resolved, and these results confirmed the validity of the new approach for estimating the indented surface area and the stretch strain.

5. CONCLUSIONS

Spherical indentation was adopted for surface-local characterization of the indentation strain for several microindents formed on a Zr-based metallic glass. Instead of the conventional indentation strains, the stretch strain proposed by Milman *et al.* was adopted in this study. However, the indented surface area calculated from the Riemann integral resulted in a significant overestimation of the stretch strain. To avoid the troublesome pixel manipulation in the Riemann integral, a new morphological fitting method for remnant microindents was proposed in this study. A spherical microindent formed on the metallic glass was fitted into the part of the prolate ellipsoid. Equations for the axial radii and curved surface area of the ellipsoidal morphology were derived through a series of modeling. From 3D morphologies of the microindents on the Zr-based metallic glass, the stretch strains were calculated based on the Milman's definition and were compared with the indentation strains from other methods. The calculated whole stretch strains were lower than their upper limits and quantitatively close to the conventional indentation strains. Unexpected lower values of the stretch strain less than 50 μm were explained by a significant elastic recovery at the shallow indentation regime. From a general viewpoint, the strain overestimation by the Riemann integral was clearly resolved by adopting the morphological fitting model for calculating the indented surface area and the stretch strain.

ACKNOWLEDGMENTS

This research was partly supported by Converging Research Center Program(2013K000403) under the Ministry of Science, ICT and Future Planning and the Energy R&D Program (20113020010050) under the Korea Ministry of Knowledge Economy.

REFERENCES

1. A. Inoue, *Acta Mater.* **48**, 279 (2000).
2. P. E. Donovan, *J. Mater. Sci.* **24**, 523 (1989).
3. M. W. Lee, H. J. Shin, S. H. Hong, J. T. Kim, H. Choi-Yim, Y. Seo, W. H. Lee, P. Yu, M. Qian, J. K. Lee, and K. B. Kim, *Met. Mater. Int.* **20**, 1 (2014).
4. W. J. Wright, R. Saha, and W. D. Nix, *Mater. Trans. JIM* **42**, 642 (2001).
5. M. N. M. Patnaik, R. Narashimhan, and U. Ramamurty, *Acta Mater.* **52**, 3335 (2004).
6. D. Tabor, *Rev. Phys. Technol.* **1**, 145 (1970).
7. V. Keryvin, *Acta Mater.* **55**, 2565 (2007).
8. K. Ai and L. H. Dai, *Scr. Mater.* **56**, 761 (2007).
9. J.-H. Ahn and D. Kwon, *J. Mater. Res.* **16**, 3170 (2001).
10. C. Tang, Y. Li, and K. Zeng, *Mater. Sci. Eng. A* **384**, 215 (2004).
11. Y.-H. Lee, H.-Y. Yu, U. B. Baek, and S. H. Nahm, *Kor. J. Met. Mater.* **48**, 203 (2010).
12. B. T. Jang, S. S. Kim, and S. Yi, *Met. Mater. Int.* **20**, 55 (2014).
13. Y. V. Milman, B. A. Galanov, and S. I. Chugunova, *Acta Metall. Mater.* **41**, 2523 (1993).
14. Y.-H. Lee, J. S. Park, H. M. Lee, and S. H. Nahm, *Int. J. Mod. Phys. B* **24**, 2453 (2010).
15. V. A. Kumar and S. Mathew, *Biosys. Eng.* **85**, 1 (2003).
16. W. C. Oliver and G. M. Pharr, *J. Mater. Res.* **7**, 1564 (1992).
17. Y. Y. Lim, M. M. Chaudhri, and T. Enomoto, *J. Mater. Res.* **14**, 2314 (1999).
18. K. Sangwal, P. Gorostiza, J. Servat, and F. Sanz, *J. Mater. Res.* **14**, 3973 (1999).
19. R. Saha and W. D. Nix, *Mater. Sci. Eng. A* **319-321**, 898 (2001).
20. D. Beegan, S. Chowdhury, and M. T. Laugier, *Surface Coat. Technol.* **176**, 124 (2003).
21. K. Kese and Z. C. Li, *Scr. Mater.* **55**, 699 (2006).
22. Y.-H. Lee, J. H. Hahn, S. H. Nahm, J.-I. Jang, and D. Kwon, *J. Phys. D: Appl. Phys.* **41**, 074027 (2008).